Performance of X-Ray Photon-Counting Scintillation Detectors Under Pile-Up Conditions at 60 keV

Van Der Sar, Stefan J.; Schaart, Dennis R.

DOI
10.1109/TRPMS.2025.3532592

Publication date
2025

Document Version
Final published version

Published in
IEEE Transactions on Radiation and Plasma Medical Sciences

Performance of X-Ray Photon-Counting Scintillation Detectors Under Pile-Up Conditions at 60 keV

Stefan J. van der Sar and Dennis R. Schaart, *Senior Member, IEEE*

***Abstract*—We investigate silicon photomultiplier (SiPM)-based scintillation detectors for medical X-ray photon-counting applications, where the input count rate (ICR) can reach a few Mcps/mm^2 in cone-beam CT for radiotherapy, for example, up to a few hundred Mcps/mm^2 in diagnostic CT. Thus, pulse pile-up can severely distort the measurement of counts and energies. Here, we experimentally evaluate the counting and spectral performance of SiPM-based scintillation detectors at 60 keV as a function of ICR/pile-up level. We coupled 0.9×0.9×3.5 mm^3 LYSO:Ce and 0.9×0.9×4.5 mm^3 YAP:Ce scintillators to 1.0×1.0 mm^2 ultrafast SiPMs and exposed these single-pixel detectors to a 10-GBq Am-241 source. We varied ICR from 0 to 5 Mcps/pixel and studied detector performance for paralyzable-like (p-like) and nonparalyzable-like (np-like) counting algorithms, after applying a second-order low-pass filter with cut-off frequencies f_c of 5, 10, or 20 MHz to the pulse trains. Counting performance was quantified by the output count rate (OCR) and the count-rate loss factor (CRLF). In addition to the traditional spectral performance measure of the full-width-at-half-maximum (FWHM) energy resolution at low ICR, we propose the spectral degradation factor (SDF) to quantify spectral effects of pile-up at any ICR. Best counting performance is obtained with np-like counting and $f_c = 20$ MHz, for which the count-rate loss is at most 10% in the investigated range of ICRs, whereas p-like counting yields best spectral performance. Due to less pile-up, the fastest pulses obtained with $f_c = 20$ MHz already provide the best SDF values at ICRs of a few Mcps/pixel, despite their worse low-rate energy resolution. Hence, spectral performance under pile-up conditions appears to benefit more from substantially faster pulses than a somewhat better low-rate energy resolution. Moreover, we show that the pulse shape of SiPM-based detectors allows to improve spectral performance under pile-up conditions using *dedicated peak detection windows*.**

***Index Terms*—Energy resolution, silicon photomultiplier (SiPM), spectral degradation.**

Received 29 October 2024; revised 3 December 2024; accepted 23 December 2024. Date of publication 22 January 2025; date of current version 4 July 2025. *(Corresponding author: Dennis R. Schaart.)*

This work did not involve human subjects or animals in its research.

Stefan J. van der Sar is with the Department of Radiation Science and Technology, Delft University of Technology, 2629 JB Delft, The Netherlands (e-mail: s.j.vandersar@tudelft.nl).

Dennis R. Schaart is with the Department of Radiation Science and Technology, Delft University of Technology, 2629 JB Delft, The Netherlands, and also with Holland Proton Therapy Center, 2629 JH Delft, The Netherlands (e-mail: d.r.schaart@tudelft.nl).

This article has supplementary material provided by the authors and color versions of one or more figures available at https://doi.org/10.1109/TRPMS.2025.3532592.

Digital Object Identifier 10.1109/TRPMS.2025.3532592

I. Introduction

THE development of photon-counting detectors (PCD) as an alternative to energy-integrating detectors for medical X-ray imaging, in particular for X-ray computed tomography (CT), has become a hot topic of research [1], [2], [3]. These detectors aim to count the number of incident X-ray photons and to measure the energy of each of these photons, thereby enabling improvements in image quality (contrast-to-noise ratio) and creating opportunities for spectral imaging beyond dual-energy techniques.

In medical X-ray imaging, tube voltages up to 150 kV are used and the PCDs under development assign the detected photons to one of a few energy bins that span the X-ray tube spectrum. A major challenge is the photon fluence rate incident on the detector, which can reach a few million photons/s/mm^2 in cone-beam CT in radiotherapy (see Supplemental Materials), for example, up to a few hundred million photons/s/mm^2 in diagnostic CT [4]. Prototype diagnostic PCD-CT systems are therefore equipped with direct-conversion detectors based on the semiconductors CdTe [5], $Cd_{1-x}Zn_xTe$ (CZT, x typically 0.1 or 0.2) [6], or Si [7], as this type of detector provides a fast detector pulse (tens of nanoseconds wide) in response to an X-ray photon and enables relatively easy fabrication of miniaturized pixels (smaller than 0.5 × 0.5 mm^2), so that the negative effects of pulse pile-up on the measurement of counts and energies can be mitigated to some extent.

In a direct-conversion detector, an X-ray photon releases electron-hole pairs, which travel to opposite electrodes under the influence of an electric field, thereby inducing current pulses. A pixelated detector is obtained by dividing one of the electrodes into small elements, the pitch of which sets the pixel size. Stable and reliable performance of such semiconductor detectors requires good and uniform charge transport characteristics. However, issues with the cost-effectiveness of growing CdTe and CZT of the required quality may remain [1], [8]. In addition, the number of manufacturers that can synthesize these high-quality materials is limited. Si does not have these drawbacks, but it has a low mass density (ρ = 2.3 gcm^{-3}) and atomic number (Z = 14) for hard X-ray applications. It thus remains unclear what the best choice of detector is, leaving room for developing other types of detector.

We are investigating detectors based on scintillators and silicon photomultipliers (SiPM) as an alternative to

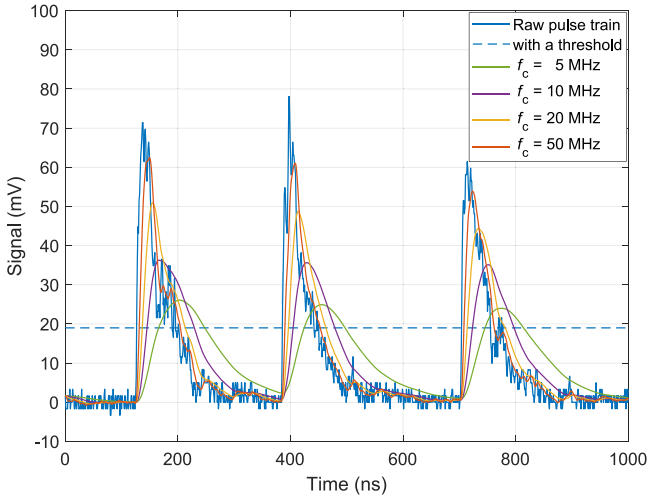

Fig. 1. Example of a part of a raw pulse train measured with the LYSO:Ce detector and its second-order low-pass filtered versions for cut-off frequencies f_c equal to 5, 10, 20, and 50 MHz. The higher f_c, the smaller the pulse amplitude loss and the faster the pulses. For example, the full-width at tenth maximum of the pulses from this LYSO:Ce detector decreases on average from 230 to 132 ns when f_c is increased from 5 to 20 MHz. The figure shows three samples of such pulse shortenings. On the other hand, the fluctuations on the pulses are less dampened by filters with a higher value of f_c, as can be seen on the three pulses for $f_c = 50$ MHz. An exemplary count detection threshold for the raw pulse train is also shown. This threshold level varies with f_c. See Section II-C for how we determined these levels.

direct-conversion detectors [9], [10]. SiPM-based scintillation detectors rely on indirect conversion, i.e., an X-ray photon absorbed in a scintillation crystal is converted into optical photons, which are in turn converted into a current pulse by an SiPM. Such a crystal-SiPM pair forms a detector pixel. A pixelated detector is obtained by optically coupling an array of crystals to an array of SiPMs with equal pitch. Thin layers of reflective material (tens of microns [11], [12]), on top of and between crystals ensure optimal light collection within each pixel and prevent light sharing between crystals. Alternative methods for light confinement to a pixel, not relying on X-ray insensitive reflectors, exist or are being (further) developed [13], [14]. Whereas direct-conversion detectors can suffer from spectral degradation due to charge sharing among pixels, scintillation detectors with good light confinement do not suffer from a similar degradation due to light sharing. Scintillator-based PCDs may therefore enable better performance in spectral imaging tasks, such as water–bone material decomposition and K-edge imaging [15].

To a first approximation, the number of scintillation photons N detected by the SiPM is proportional to the energy deposited by the X-ray photon (in the order of 10^0-10^1 photons/keV), while the probability that an optical photon is detected at a time t_0 after the interaction of the X-ray photon is proportional to $\exp(-t_0/\tau_d)$, with τ_d the decay time constant of the scintillator. A detected scintillation photon triggers an avalanche multiplication process in one of the single-photon avalanche diodes (SPAD) of the SiPM. This results in a current pulse, which is called the single-SPAD response (SSR). It can be described as $G{\cdot}\exp(-(t-t_0)/\tau_r)$ with $t-t_0 \geq 0$, τ_r the recharge time constant of the SiPM, and the gain G equal to the total number of electrons (typically in the order of 10^5-10^6). Thus, a detected X-ray photon results in a current pulse that follows the convolution of two decaying exponentials with time constants τ_d and τ_r, the pulse height (or integral $N{\cdot}G$) of which is a measure of the energy deposited by the X-ray photon [9], [10]. However, such a pulse is subject to statistical fluctuations due to the stochastic emission times of the relatively few scintillation photons detected per unit time (see blue curve in Fig. 1). The more detected scintillation photons per unit time, the lower the level of pulse fluctuations.

The gain of the SiPM allows for a pulse processing chain in each pixel only consisting of current-to-voltage conversion that maintains the raw pulse shapes, a low-pass filter, which attenuates the statistical fluctuations on the raw pulses, and comparators and counters. This is a simpler pulse processing chain than needed in direct-conversion detectors [16].

In this work, we evaluate different filtering and counting methods for the combined measurement of counts and energy, not only at low fluence rates but also under pile-up conditions, which can be expected in (medical) X-ray photon-counting applications. To this end, we conduct experiments in which we gradually increase the input count rate (ICR), i.e., the number of X-ray photons that deposit energy in the detector per unit time, and quantify the counting performance and spectral performance of each method as a function of ICR. We make use of $1{\times}1$ mm^2 single-pixel detectors and a 10-GBq Am-241 source of 60-keV photons. Such a mono-energetic source makes it more straightforward to evaluate spectral performance than a poly-energetic beam from an X-ray tube, because the true energy of every photon is known a priori. However, the ICR that can be achieved with this pixel size and source is limited to about 5 Mcps. Therefore, to be able to study filtering and counting methods under pile-up conditions, we used two scintillators that are expected to show some pile-up at a few Mcps/pixel. One of them is LYSO:Ce, which, together with SiPMs, has found widespread use in detectors for clinical PET scanners [17]. As such, it is an example of a detector that can combine stable and reliable performance over time with cost-effective manufacturing. The other is YAP:Ce, which has not found use in clinical imaging systems yet. Nevertheless, it is a readily available and has a somewhat smaller decay time constant than LYSO:Ce, potentially increasing the count-rate capability [9], [10]. Moreover, we highlight that faster scintillators than YAP:Ce exist, such as $LaBr_3$:Ce, which seem suitable for more demanding X-ray photon-counting applications in terms of ICR [18].

II. Materials and Methods

A. Data Acquisition

We built two single-pixel detectors by optically coupling a $0.9 \times 0.9 \times 3.5$ mm^3 $Lu_{1.8}Y_{0.2}SiO_5$:Ce scintillation crystal (LYSO:Ce, $\rho = 7.1$ g/cm^3, Shanghai Project Crystal) and a $0.9 \times 0.9 \times 4.5$ mm^3 $YAlO_3$:Ce scintillation crystal (YAP:Ce, $\rho = 5.4$ g/cm^3, Crytur) to 1.0×1.0 mm^2 SiPMs (Broadcom Inc.) using Norland Optical Adhesive 63 and Norland Optical Adhesive 88, respectively. We selected these adhesives, because their transmission spectra match

well with the emission spectra of the scintillators. We then submerged the crystals in reflective polytetrafluoroethylene (PTFE, Teflon) powder, which we compressed to increase the light collection on the SiPMs.

The SiPMs are based on Broadcom's near-ultraviolet high-density (NUV-HD) technology and feature a SPAD pitch of 15 μm and an ultrafast SSR with a recharge time constant $\tau_r = 7$ ns. Consequently, the SSR will hardly elongate the raw detector pulses if the scintillator is LYSO:Ce or YAP:Ce, for which we measured decay time constants τ_d of 33 ns (LYSO:Ce) and 29 ns (YAP:Ce) following the method described in [19]. Furthermore, the probability of crosstalk between SPADs is low (<10%), and afterpulsing is negligible. However, the photodetection efficiency (PDE) is only between 20% and 30% in the relevant wavelength range. Information about the definitions of these SiPM characteristics can be found elsewhere, e.g., in [20].

We exposed the detectors to a 10-GBq Am-241 source that effectively functions as a mono-energetic source of 60-keV photons, because its lower-energy photon emissions are mostly absorbed by the source window. By varying the source–detector distance (SDD), we were able to study the detector performance for various ICRs and pulse pile-up levels. It should be noted that the crystal thicknesses of 3.5 mm (LYSO:Ce) and 4.5 mm (YAP:Ce) were not selected with a specific X-ray detection efficiency or imaging application in mind, but because they allowed the top face of the crystals to be very close to the source window, which was a few mm recessed into the source housing. This helped to increase the ICRs achievable with this source.

The detectors were mounted on Broadcom's AFBR-S4E001 evaluation board that contains a 166 V/A amplification stage, which preserves the raw pulse shapes. The board's output was fed into a Teledyne LeCroy HDO9409 digital oscilloscope operating at a bandwidth of 200 MHz and a sampling rate of 1 GS/s. In this way, ten pulse trains of 100 ms were digitized for each detector and SDD. Various processing methods were then applied to the digitized pulse trains. They are described in more detail in the next two subsections. However, we first checked, for both detectors, if there was any (constant) baseline shift in the pulse trains measured at the longest SDD, i.e., with virtually no pile-up present. Such offsets may be caused by offsets in the front-end electronics, for example. If so, we subtracted that offset from all pulse trains measured with that detector, i.e., also from those measured at shorter SDDs. In this way, any possible degradation of counting and spectral performance caused by additional, pile-up induced baseline shifts at shorter SDDs remains uncorrected for in this work.

B. Pulse Processing I: Second-Order Low-Pass Filters

As will become clear in Section II-C, the detection of a count is usually associated with the signal from the detector exceeding a threshold value. Fig. 1 shows that the fluctuations on the raw detector pulses may cause a pulse to cross such a threshold more than once, which could lead to counting a single X-ray photon multiple times. Moreover, the fluctuations negatively affect the pulse height (i.e., energy) resolution.

The use of low-pass filters is a straightforward and practical way to get rid of these pulse fluctuations. Such filters are characterized by their cut-off frequency f_c. A filter with a lower value of f_c more strongly reduces the fluctuations on the pulses, but also gives rise to more amplitude loss and pulse elongation. Vice versa, we expect higher count rate capability, but worse energy resolution from a filter with a higher value of f_c. The number of low-pass filters applied in succession is called the order of the filter. Higher-order filters achieve a given remaining level of pulse fluctuations at higher values of f_c than a first-order filter, resulting in faster but equally smooth pulses. As such, they seem well suited for high-rate X-ray photon-counting applications. However, higher-order filters also lead to more pulse amplitude loss, so the useful range of filter orders is limited, and we only worked with second-order low-pass filters in this study.

Fig. 1 shows a snapshot of a raw pulse train and the effect of applying filters with various values for f_c. In a histogram of the maximum signal recorded between each positive and the subsequent negative crossing of the count detection threshold in such a pulse train, a too high level of pulse fluctuations appears as a peak just above the threshold value (see Section II-C for how we determined these thresholds for each value of f_c). We found that this peak remained absent up to values of f_c of around 20 MHz, for both the LYSO:Ce and the YAP:Ce detector. For higher values of f_c, e.g., 50 MHz, some remaining fluctuations on the falling edges of the pulses can indeed be observed in Fig. 1. We also found that the pulse amplitude loss became too large for values of f_c less than 5 MHz. We therefore studied second-order low-pass filters with three values of f_c, namely, 5, 10, and 20 MHz.

All filters were implemented in the time domain. The differential equation that describes how the output voltage V_{out} of a first-order low-pass filter depends on the input voltage V_{in}, the time derivative of V_{out} and f_c reads

$$V_{out}(t) = V_{in}(t) - \frac{1}{2\pi f_c}\frac{dV_{out}}{dt}. \quad (1)$$

This was discretized into the following form using the backward differentiation method:

$$V_{out}[n] = \frac{2\pi f_c \Delta t}{1 + 2\pi f_c \Delta t} V_{in}[n] + \frac{1}{1 + 2\pi f_c \Delta t} V_{out}[n-1]. \quad (2)$$

Here, n indicates the sample number and Δt the sampling period (1 ns in our case as the sampling rate of the digital oscilloscope was 1 GS/s). We applied (2) twice to emulate the effect of a second-order filter.

C. Pulse Processing II: Counting Algorithms

We implemented two counting algorithms to extract energy-resolved photon-counting data from the filtered pulse trains. These algorithms are described in the following.

Paralyzable-Like (p-like) Counting: A count is registered when a filtered pulse train causes a positive crossing of a threshold. We call the maximum signal between this positive threshold crossing and the subsequent negative threshold

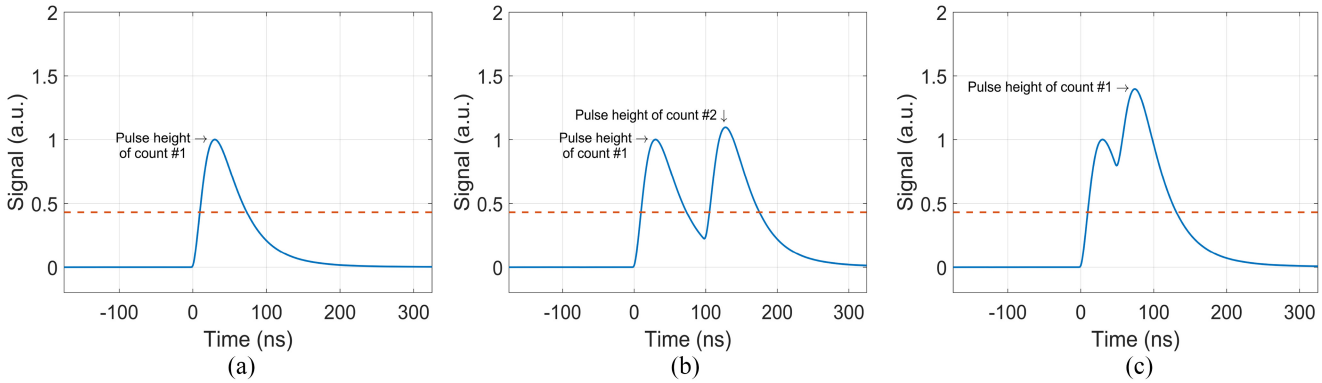

Fig. 2. (a) p-like counting algorithm registers a count when a positive threshold (dashed line) crossing takes place. The maximum signal before the next negative threshold crossing is considered the pulse height of that count and therefore a measure of the energy deposited by the absorbed 60-keV photon. (b) When a pulse piles up on the tail of a previous one, the pulse height associated with the second count is distorted. (c) When a pulse is generated before the previous one has decayed to below the threshold level, only one count is registered and the pulse height of that count is distorted.

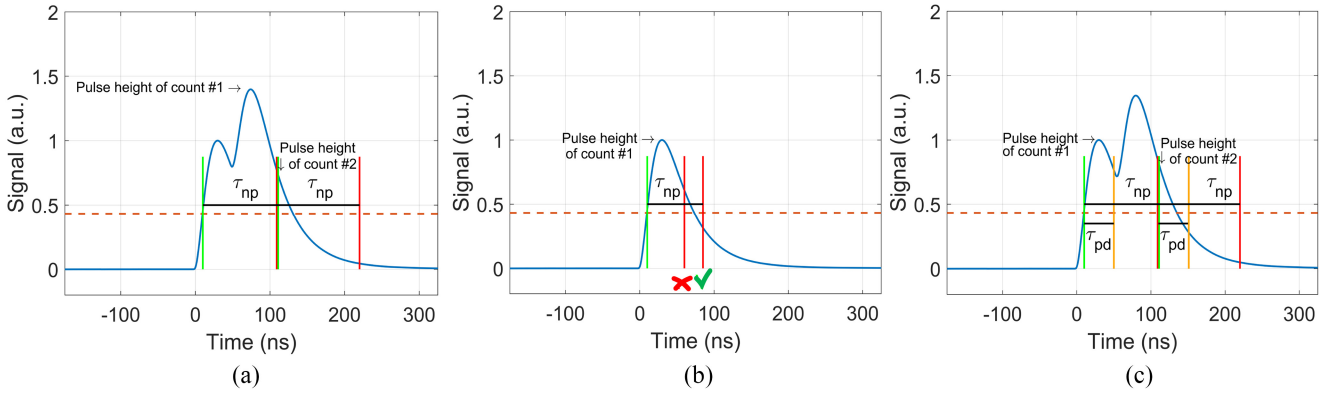

Fig. 3. (a) np-like counting algorithm evaluates, at the end of a window of length τ_{np} following a positive threshold crossing, if the signal is still above threshold (dashed line) or not. If so, a second count is registered and a new window of length τ_{np} is started, and so on. The maximum signal within each window is considered the pulse height associated with that count. Although this algorithm allows to correctly count the number of pulses, the pulse height measurement is still distorted. (b) It is very important that τ_{np} exceeds the time-over-threshold of the pulses, so that no two counts are registered for a single pulse. (c) Pulse height measurement may be improved by determining the maximum signal within a shorter peak detection window of length τ_{pd} starting at the beginning of the window of length τ_{np}. Note that this dedicated peak detection window can also be implemented in the p-like algorithm.

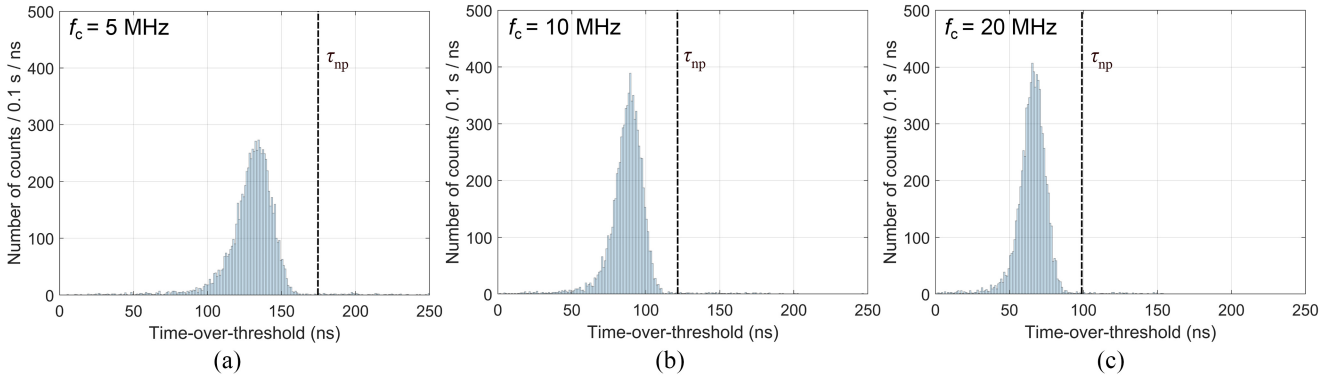

Fig. 4. ToT histograms (bin width = 1 ns; measurement time = 100 ms) for the LYSO:Ce detector and cut-off frequencies f_c of the second-order low-pass filter applied to the raw pulse trains equal to (a) 5 MHz, (b) 10 MHz, and (c) 20 MHz. The values for τ_{np} of the np-like counting algorithm were set to 110% of the ToT values corresponding to the right-hand sides of the peaks, i.e., 176 ns for $f_c = 5$ MHz, 121 ns for $f_c = 10$ MHz, and 99 ns for $f_c = 20$ MHz, as visualized by the dashed lines in the diagrams.

crossing the pulse height [see Fig. 2(a)]. It is usually a good measure of the energy deposited by the X-ray photon. However, if a pulse piles up on the tail of the previous pulse, as shown in Fig. 2(b), the pulse height yields an erroneous measurement of the energy. Furthermore, if an X-ray photon interacts in the detector before the previous pulse has dropped below the threshold level, the new pulse will not cause a positive threshold crossing and only one count, with an incorrect energy, is registered [see Fig. 2(c)]. This type of counting gives rise to paralyzable-like behavior, which means

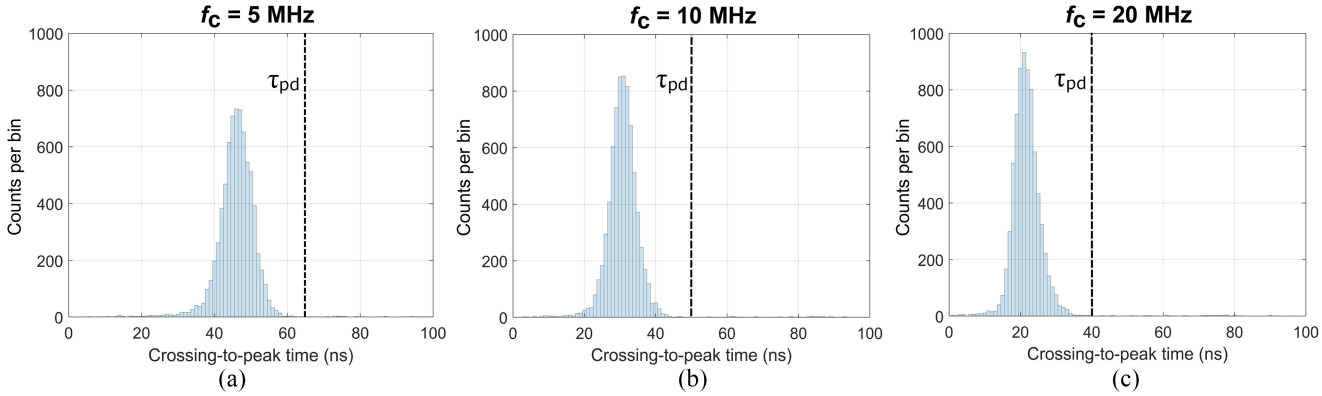

Fig. 5. (Positive threshold) crossing-to-peak time histograms (bin width = 1 ns; measurement time = 100 ms) for the LYSO:Ce detector and cut-off frequencies f_c of the second-order low-pass filter applied to the raw pulse trains equal to (a) 5 MHz, (b) 10 MHz, and (c) 20 MHz. The lengths τ_{pd} of the dedication peak detection windows were chosen such that all pulses reach their peak in this period of time, i.e., 65 ns for f_c = 5 MHz, 50 ns for f_c = 10 MHz, and 40 ns for f_c = 20 MHz, as visualized by the dashed lines in the diagrams.

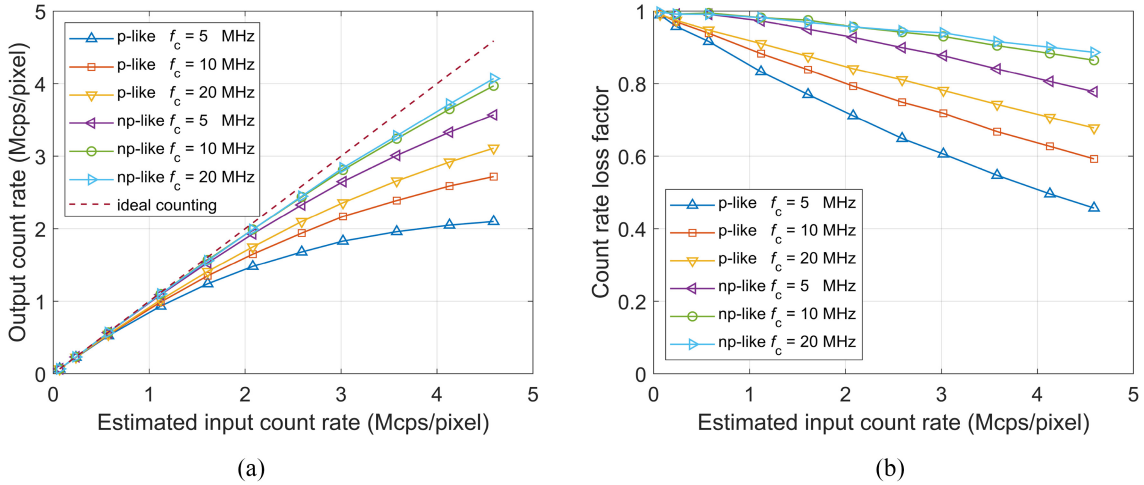

Fig. 6. (a) OCR of the LYSO:Ce detector as a function of the estimated ICR, the cut-off frequency f_c of the second-order low-pass filter applied to the raw pulse trains, and the counting algorithm (p-like or np-like). The line labeled "ideal counting" is defined as OCR = ICR. (b) CRLF, defined as OCR divided by estimated ICR for a given algorithm and value of f_c, as a function of ICR.

that the number of registered counts per unit time, i.e., the output count rate (OCR), is proportional to the ICR at low values of ICR, but starts to deviate at higher values, until it reaches a maximum. The OCR then starts to decrease and approaches zero for very high values of ICR. In that case, the pulse train is above threshold almost all the time, so hardly any threshold crossings occur, and hardly any counts are registered.

In this work, we set the count detection threshold to a voltage level equivalent to about 25 keV, which we calculated for each value of the filter cut-off frequency by multiplying the mean pulse height (unit: mV) corresponding to the detection of a 60-keV photon from the Am-241 source by a factor 25 keV / 60 keV $\approx$ 0.4167. We determined this mean pulse height from a Gaussian fit to the histogram of pulse height values measured at the longest SDD with that cut-off frequency. Thresholds in the range of 20–30 keV are commonly implemented in CdTe- and CZT-based PCDs for diagnostic CT, because they are above the noise floor of these detectors and at the lower end of the (hardened) X-ray tube spectra typically used in this application. It is noted that spectral PCDs additionally have multiple higher (often adjustable) thresholds. These are only used to assign the counts to energy bins, and do not limit the count rate capability of the detectors [21], [22], so they are not of interest to this study.

The peak in each pulse height histogram measured with the YAP:Ce detector was found to be asymmetric, mainly due to K-escape events. We therefore fitted two Gaussians through such peaks, one representing the photopeak (60 keV), the other the K-escape peak. Since the energy of the K X-rays of yttrium (Y) is about 15 keV, the K-escape peak is located around 45 keV. We therefore implemented a constraint that the Gaussian corresponding to the K-escape peak must be centered around 45 keV/60 keV$\times$100% = 75% of the mean value of the Gaussian corresponding to the photopeak. (An example of such an asymmetric peak with double Gaussian fit is shown in Fig. 7.)

Nonparalyzable-Like (np-like) Counting: A np-like counting algorithm allows to register two counts for the superposition of the two pulses in Fig. 2(c). It can be implemented by evaluating, after a fixed time period of length τ_{np} following a

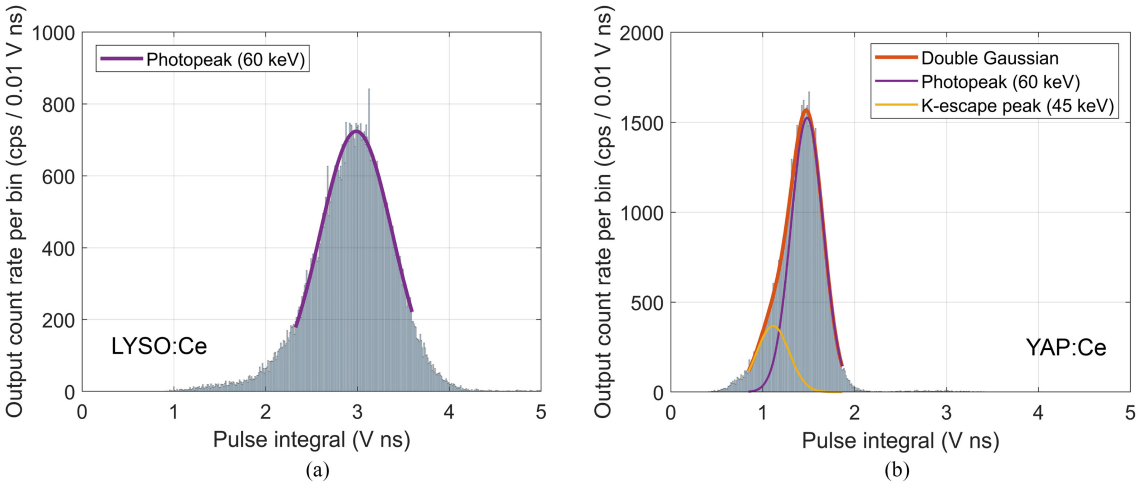

Fig. 7. Pulse integral histograms determined using the GS method explained in Section II-D for (a) LYSO:Ce detector and (b) YAP:Ce detector. Despite yielding an approximately twice as weak scintillation signal, the YAP:Ce detector provides a somewhat better energy resolution (28% versus 31% FWHM at 60 keV) due to its better proportionality [26]. Details about the double Gaussian fit in (b) are given in Section II-C. The double Gaussian is the sum of the Gaussians representing the photopeak and the K-escape peak.

positive threshold crossing (the first count), whether or not the pulse train is still above threshold [23]. If so, a second count is registered and the same evaluation will be repeated after another period of length τ_{np} [see Fig. 3(a)]. If the outcome of the evaluation is negative, the next count is only registered when the next positive threshold crossing occurs. In the case of very high ICR, the pulse train is above threshold more or less all the time, so the outcome of almost every evaluation is positive, and OCR approaches an asymptotic value of $1/\tau_{np}$. This is nonparalyzable behavior. We refer to the maximum signal within a time window of length τ_{np} as the pulse height and consider it a measure of the energy associated with the corresponding count. Distorted energy measurements are therefore still possible under pile-up conditions [see Fig. 3(a)].

It is important that τ_{np} exceeds the time-over-threshold (ToT) of the pulses in order to prevent double counting of a single X-ray photon, as visualized in Fig. 3(b). We therefore created histograms of the ToT of all pulses registered as counts by the p-like algorithm at the longest SDD, for all three values of f_c and for both detectors. The histograms, which are shown in Fig. 4 for the LYSO:Ce detector and in the Supplemental Materials for the YAP:Ce detector, contain a dominant peak, which means that (almost) all pulses have a ToT less than a certain ToT_{max}, i.e., the ToT corresponding to the right-hand side of the peak. We defined τ_{np} to be 110% of ToT_{max} in order to ensure that, in the case of pile-up, when the ToT of the second pulse may be elongated, the algorithm still registers two counts instead of three. The values of τ_{np} obtained in this way can be found in Table I, and are visualized by the vertical dashed lines in Fig. 4 (LYSO:Ce) and the Supplemental Materials (YAP:Ce). The faster scintillation decay of YAP:Ce (see Section II-A) explains the lower values for this detector.

D. Performance Measure I: Spectral

We first determined the best achievable spectral performance of the two detectors, at low ICR, using a digital signal processing technique that may not be trivial to implement in practical imaging systems with a high channel density. This method is referred to as the "gold-standard (GS) method" in this work. We filtered the pulse trains recorded at the longest SDD using a median filter of 21st order. Such a filter preserves the steep rising edges of the raw detector pulses, but still suppresses the fluctuations on these pulses. The median filtered pulse trains can therefore be used to determine accurately the number of pulses in the pulse train and the timestamp of the positive threshold crossing of each pulse. After the timestamps had been determined, each raw pulse was numerically integrated for a subsequent period of time equal to five times the scintillation decay time constant τ_d. We fitted a Gaussian through the photopeak in a histogram of pulse integral values in order to determine the energy resolution as the ratio of the full width at half maximum (FWHM $= 2.355\sigma$, with σ the standard deviation of the Gaussian) and the mean pulse integral μ. It is noted that, in the case of the YAP:Ce detector, a double Gaussian was fitted under the constraint described in Section II-C in order to account for K-escape events. In this case, σ and μ of the Gaussian corresponding to the photopeak were used to determine the energy resolution. The results can be considered the best FWHM energy resolutions achievable with these detectors, as $> 99\%$ of the scintillation photons are collected on the SiPM within this $5\tau_d$ window.

At higher ICRs, pulse pile-up will cause counts to end up outside the photopeak. Under such conditions, the FWHM energy resolution no longer provides a full description of the spectral performance of a detector. We therefore propose an additional metric, the spectral degradation factor (SDF), which can be calculated in the following way.

Step 1: For a given detector and the GS method (applied at the longest SDD), determine the fraction of all counts that fall within a bin centered on the mean pulse integral μ_{GS} with a width equal to the FWHM_{GS} of the Gaussian distribution of pulse integrals in the photopeak. Call this fraction the GS FWHM fraction P_0. Furthermore, calculate the GS energy

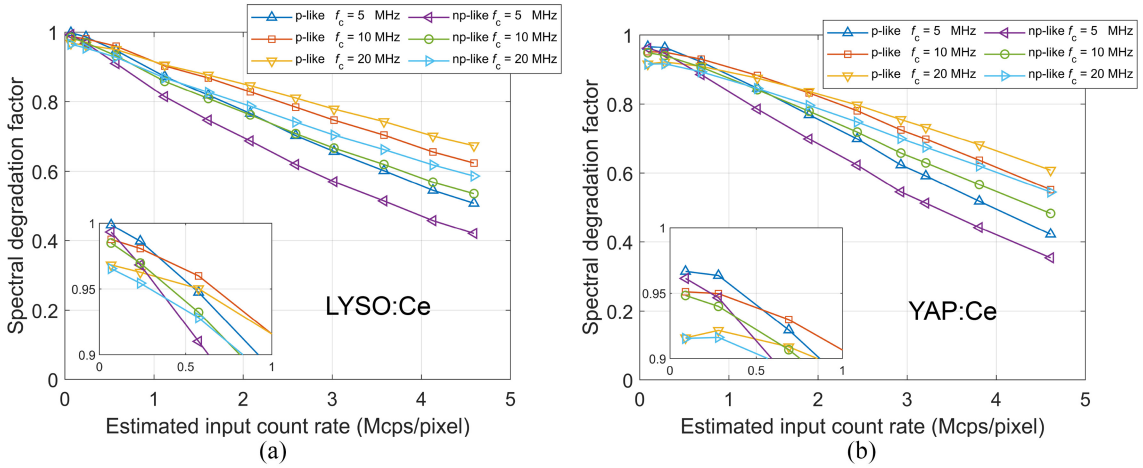

Fig. 8. (a) SDF of the LYSO:Ce detector, for which $P_0 = 0.723$ [see (5)], as a function of the estimated ICR, the counting algorithm (p-like or np-like), and the cut-off frequency f_c of the second-order low-pass filter applied to the raw pulse trains. (b) Corresponding data set for the YAP:Ce detector, for which $P_0 = 0.638$. This lower value of P_0 is mainly due to K-escape events in the YAP:Ce detector.

TABLE I
VALUES FOR THE PARAMETERS τ_{np} AND τ_{pd} USED IN THIS WORK. SEE SECTIONS II-C AND II-D AND FIGS. 4 AND 5 FOR MORE INFORMATION ON THE MEANING OF THESE PARAMETERS AND HOW THEY WERE DETERMINED

	LYSO:Ce		YAP:Ce	
f_c (MHz)	τ_{np} (ns)	τ_{pd} (ns)	τ_{np} (ns)	τ_{pd} (ns)
5	176	65	170	65
10	121	50	115	50
20	99	40	88	40

resolution R_{GS} as

$$R_{GS} = \frac{\text{FWHM}_{GS}}{\mu_{GS}}. \tag{3}$$

Step 2: For a given pulse processing method (value for f_c of the low-pass filter and p-like or np-like counting), calculate a bin width W_{PPM} as

$$W_{PPM} = R_{GS} \times \mu_{PPM}. \tag{4}$$

Here, μ_{PPM} is the mean pulse height in the photopeak for that pulse processing method at the longest SDD, obtained with either a single or double Gaussian fit to the pulse height histogram (as argued in Section II-C). Center a bin of width W_{PPM} on μ_{PPM} and call it the method's FWHM bin.

Step 3: For a given SDD, determine the fraction of counts that fall within the method's FWHM bin. Call this fraction the FWHM fraction and denote it as P_{FWHM}.

Step 4: Calculate the SDF as

$$\text{SDF} = \frac{P_{FWHM}}{P_0}. \tag{5}$$

The P_{FWHM}, and therefore the SDF, of a given detector provides insight into the fraction of full-energy events that can be considered correctly classified as such, both under low and high pile-up conditions. The advantage of the SDF is that the contributions to spectral degradation already contained in P_0, such as the number of K-escape and Compton scattering events and the width of the photopeak under low pile-up conditions, are canceled out. As such, the value of the SDF is always close to 1 at low ICR and does not depend on, e.g., scintillator dimensions and probe energy, thereby enabling a unambiguous comparison of the different pulse processing methods as a function of ICR.

We also used the SDF concept to investigate if and how much the spectral performance improves by regarding the maximum signal within a dedicated peak detection window (DPDW) of length τ_{pd} after a positive threshold crossing (p-like counting) or after the start of a time window of length τ_{np} (np-like counting, with $\tau_{pd}<\tau_{np}$) as the pulse height associated with that count. This idea relies on the fact that the peak of a pulse (unaffected by pile-up) from an SiPM-based scintillation detector is always reached relatively early on in the pulse. Hence, when two pulses pile up, it should still be possible to determine the correct pulse height of the first pulse provided the second pulse occurs more than τ_{pd} after the first one [see Fig. 3(c)]. In order to choose proper values of τ_{pd}, we generated histograms of the time differences between the moment each pulse crosses the threshold and the moment it reaches its maximum value determined by the p-like counting algorithm applied to the measurement at the longest SDD. Fig. 5 shows that these crossing-to-peak times have a Gaussian-like distribution, that they reduce with increasing cut-off frequency f_c, and that we selected values of τ_{pd} that correspond to the right-hand side end points of these distributions. The selected values are the same for both detectors and can be found in Table I. In the remainder of this work, we refer to this method as p/np-like counting with a DPDW. It can be implemented in practical detectors using clocked comparators, for example [24].

E. Performance Measure II: Counting

For counting photons, we first evaluated the number of registered counts per unit time, which we refer to as the OCR. Instead of studying this quantity as well as the spectral performance measures as a function of SDD, it is more

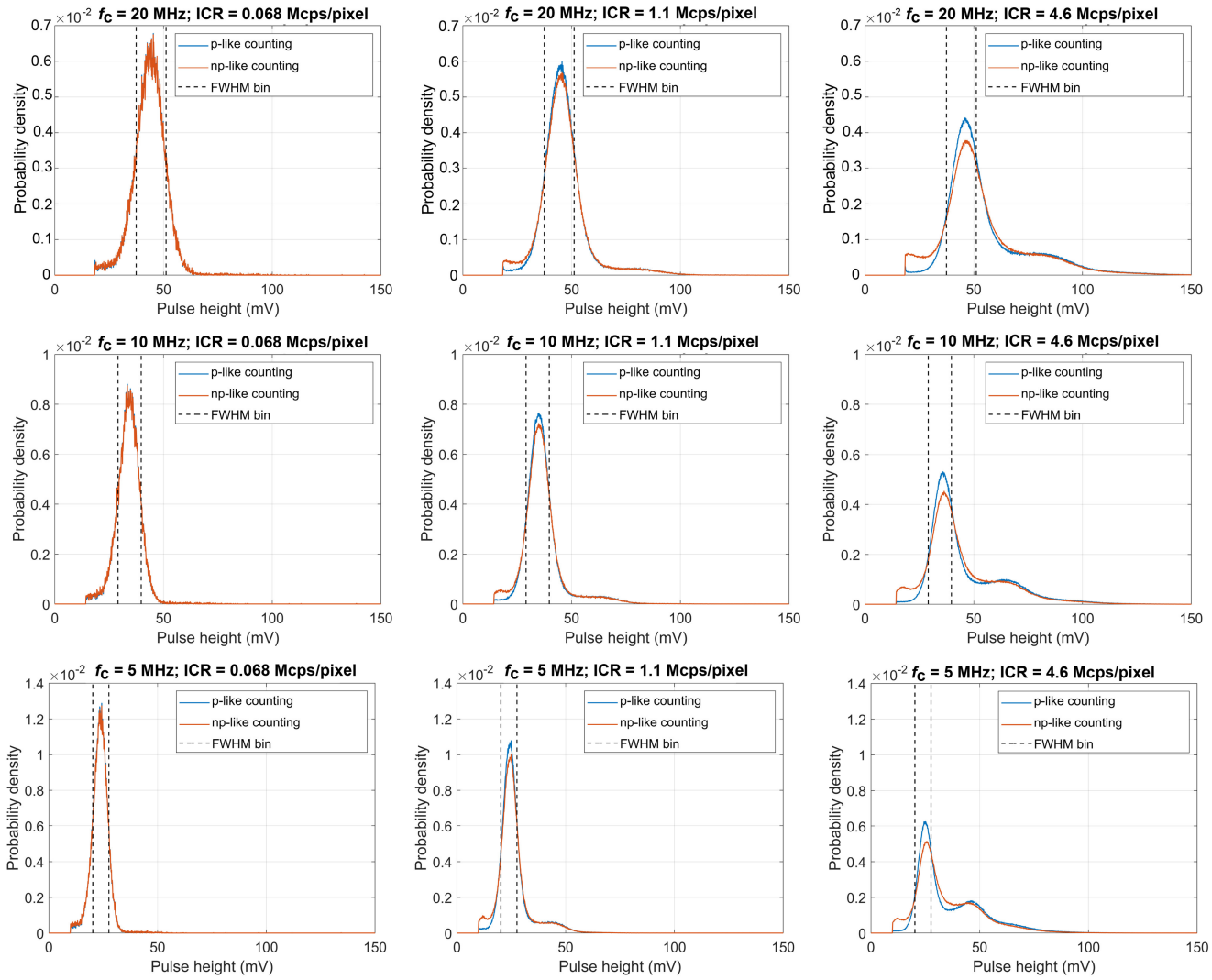

Fig. 9. Normalized pulse height spectra, which represent the probability that a registered count gets associated with a certain pulse height, measured with the LYSO:Ce detector and both the paralyzable-like and nonparalyzable-like counting algorithm. From left to right, the estimated input count rate is increasing. From top to bottom, the cut-off frequency f_c of the second-order low-pass filter applied to the raw pulse trains is decreasing. The FWHM bin, used to calculate the SDF [see Section II-D and (5)] is visualized by means of the vertical dashed lines.

valuable to study them as a function of ICR. However, the Am-241 source is a disk source and both its active area and location within the housing are not accurately known. The active area is surely larger than the cross-sectional area of the scintillation crystals (0.9×0.9 mm^2), which, combined with the nonzero thickness of the crystals, means that, particularly for the shorter SDDs, 60-keV photons also enter the crystals through the side faces. These circumstances make it hard to use an analytic formula to determine ICR for each SDD.

We therefore performed pulse train simulations to determine which OCRs to expect for a series of ICRs. For each ICR, ten trains of delta pulses were generated. The pulse trains were 100 ms in length and had a sample period of 1 ns. The number of pulses in each train was sampled from a Poisson distribution with an expectation value equal to the product of the ICR and 0.1 s (100 ms), while the timestamp of each pulse was sampled from a uniform distribution. Each delta pulse train was convolved with the mean pulse shape determined from the low-pass filtered ($f_c = 20$ MHz) experimental data. The detection threshold was again set to a level equivalent to 25 keV and the OCR was determined using both the p-like and the np-like algorithms. The OCRs obtained for each of the ten pulse trains were then averaged. These mean OCRs were stored in a lookup table alongside their corresponding ICR. By linearly interpolating the data in this table, we estimated the ICR for each measured OCR.

It is noted that some counts registered by the YAP:Ce detector correspond to K-escape events with an energy of about 45 keV instead of 60 keV. By comparing the areas under both Gaussians of the double Gaussian fit described in Section II-C, we determined that the Gaussian centered at 45 keV contained about 15% of the total number of events in the YAP:Ce detector. We therefore made sure that 15% of the pulses in the pulse train simulations had a pulse height of only $45/60\times100\% = 75\%$ of that of the pulses corresponding to 60-keV photons.

Once the estimated ICR for each SDD was known, we determined the count-rate loss factor (CRLF), i.e., the ratio of

OCR to ICR, for each measurement at a particular SDD:

$$\text{CRLF} = \frac{\text{OCR}}{\text{ICR}}. \tag{6}$$

III. Results

A. Counting Performance

Fig. 6 shows the (mean) OCR, as well as the CRLF, as a function of estimated ICR, counting algorithm, and cut-off frequency f_c for the LYSO:Ce detector. As expected, np-like counting achieves a better CRLF, and therefore a higher (mean) OCR than p-like counting for a given value of f_c. However, the fact that np-like counting with $f_c = 5$ MHz yields an even better CRLF, and, consequently, a higher OCR than p-like counting with $f_c = 20$ MHz already for ICRs in the order of 0.1 Mcps/pixel is somewhat remarkable though. Again in accordance with expectations, higher values of f_c provide higher OCRs for a given counting algorithm. Nevertheless, the curves for np-like counting with $f_c = 10$ MHz and $f_c = 20$ MHz are remarkably close to each other. For both values of f_c, it can be appreciated that the OCR is at least about 90% of the ICR up to the maximum ICR of 4.6 Mcps/pixel that we could achieve with the present experimental setup. Very similar, although slightly better, OCRs and CRLFs were measured for the YAP:Ce detector. These plots can be found in the Supplemental Materials. The similarity is due to the small difference in the decay time constants τ_d of both scintillators (see Section II-A).

B. Spectral Performance

Fig. 7 shows the results obtained with the GS method described in Section II-D. The measured FWHM energy resolutions at 60 keV are 28% and 31% for the YAP:Ce detector and the LYSO:Ce detector, respectively. Remarkably, the energy resolution of the YAP:Ce detector is better, although the mean pulse integrals of both detectors indicate that about twice as many scintillation photons per event were detected in the LYSO:Ce detector. In general, Poisson statistics imply that the more scintillation photons are detected, the better the energy resolution. However, the so-called nonproportionality of the scintillator also affects the energy resolution [25]. The more the number of generated optical photons deviates from being proportional to the energy deposited, the larger the negative effect on the energy resolution. Whereas YAP:Ce is known to be a proportional scintillator, LYSO:Ce is rather non-proportional [26]. This should largely explain the difference in measured energy resolution observed here. We also determined from the two histograms and fits in Fig. 7 the values of P_0, i.e., the fraction of the counts detected with the GS method that fall within a bin of width FWHM centered on the mean pulse integral of the photopeak (also see Section II-D/step 1). These turned out to be 0.638 for the YAP:Ce detector, and 0.723 for the LYSO:Ce detector. The lower value for the YAP:Ce detector is mainly due to the K-escape events.

Fig. 8(a) shows the SDF [defined in (5)] as a function of estimated ICR, counting algorithm, and value of f_c for the LYSO:Ce detector. The inset shows a zoomed-in version of the data for low values of the ICR. As expected, the highest SDF at the lowest ICR is achieved for $f_c = 5$ MHz, followed by $f_c = 10$ MHz and $f_c = 20$ MHz. This is because a lower value of f_c usually implies a better FWHM energy resolution. Indeed, we determined FWHM resolutions at 60 keV of 31.6% for $f_c = 5$ MHz, 32.6% for $f_c = 10$ MHz, and 33.5% for $f_c = 20$ MHz for this particular LYSO:Ce detector. The value of 31.6% for $f_c = 5$ MHz is close to the above-mentioned FWHM energy resolution of 31% at 60 keV obtained with the GS method. However, as the ICR starts to increase, a lower pile-up level due to the faster pulses offered by a higher value of f_c starts to become more beneficial for the spectral performance than the low-rate FWHM energy resolution. For p-like counting, $f_c = 5$ MHz indeed only has the highest SDF up to ICR $\approx$ 0.3 Mcps/pixel. Then, $f_c = 10$ MHz provides the best spectral performance up to ICR $\approx$ 1.0 Mcps/pixel. If ICR > 1.0 Mcps/pixel, $f_c = 20$ MHz is optimal from a spectral point-of-view. Similar trends are observed for np-like counting, the turning points being located at ICR $\approx$ 0.2 Mcps/pixel and ICR $\approx$ 0.7 Mcps/pixel.

Similar plots for the YAP:Ce detector can be found in Fig. 8(b). The data show that the dependency of the SDF at low ICRs on the value of f_c is somewhat more pronounced for the YAP:Ce detector. Indeed, we determined that the FWHM energy resolution at 60 keV ranges from 29.5% for $f_c = 5$ MHz to 33.5% for $f_c = 20$ MHz. That is a difference of 4 percentage points, or twice the difference observed for the LYSO:Ce detector, likely because of the more proportional response of YAP:Ce discussed above in the context of Fig. 7. In addition, the pile-up level for a given ICR is slightly lower in the YAP:Ce detector due to a somewhat faster scintillation decay (see Section II-A). As a result of both facts, the turning points occur at higher values of ICR, i.e., at 0.5 and 1.7 Mcps/pixel for p-like counting and at 0.4 and 1.2 Mcps/pixel for np-like counting.

C. Optimal Cut-Off Frequency and Counting Algorithm

In summary, $f_c = 20$ MHz already provides the best spectral performance at ICR values greater than about 1 Mcps/pixel, the exact value depending on detector and counting algorithm. The spectral disadvantage of a high f_c value at low ICRs is quite small and does not appear to outweigh the advantages at higher ICRs. $f_c = 20$ MHz anyway yields the best counting performance (see Fig. 6), so the highest value of f_c that still sufficiently suppresses the pulse fluctuations is most likely optimal for most X-ray imaging applications.

The question remains whether p-like or np-like counting is to be preferred. Fig. 6 showed that np-like counting is better from a counting perspective, whereas Fig. 8 indicated that the spectral degradation for given ICR and f_c is more severe for this counting algorithm. This is visually explained in Fig. 9 (top row), which contains pulse height spectra measured by the LYSO:Ce detector, for $f_c = 20$ MHz, for both counting algorithms, and for low (0.068 Mcps/pixel), intermediate (1.1 Mcps/pixel) and high (4.6 Mcps/pixel) values of the estimated ICR. For the lowest ICR, the only feature of the spectra is the full-energy peak and the spectra for p-like counting and np-like counting fully overlap. As the ICR increases, pile-up

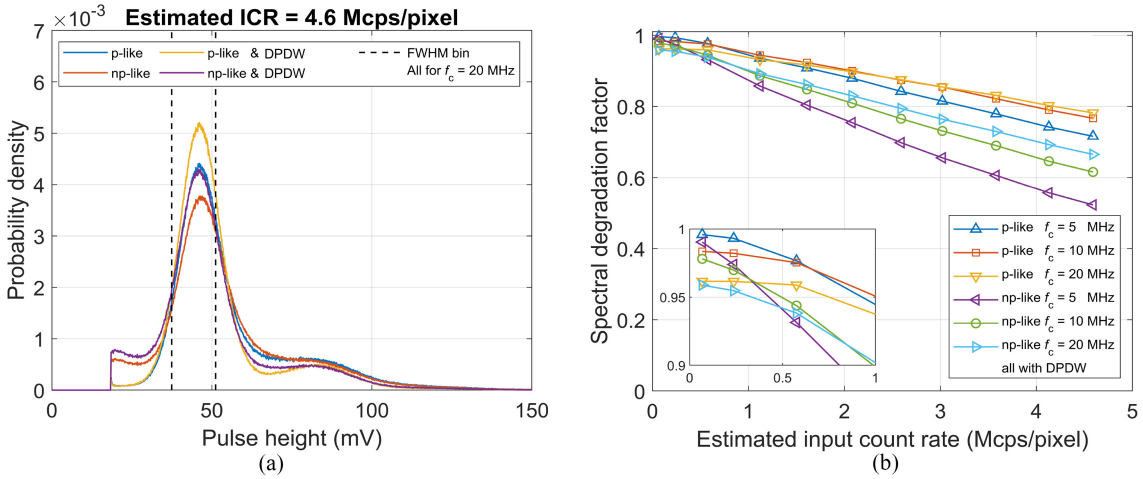

Fig. 10. (a) Effect of integrating a dedicated peak detection window into the paralyzable-like and nonparalyzable-like counting algorithms on normalized pulse height spectra, which represent the probability that a registered count has a certain pulse height. Here, spectra measured at an estimated input count rate of 4.6 Mcps/pixel with the LYSO:Ce detector and a second-order low-pass filter with a cut-off frequency $f_c = 20$ MHz are plotted with a bin width of 0.1 mV. See Section II-C and Fig. 3(c) for an explanation of the counting algorithms with a DPDW. (b) Resulting SDF [see Section II-D and (5)] as a function of ICR for the pulse processing methods with DPDW.

becomes more likely. For both p-like and np-like counting, counts affected by pile-up typically end up to the right-hand side of the FWHM bin in the pulse height spectra, thereby reducing the fraction of counts in that bin. Because of the exponential distribution of the interarrival times between two 60-keV photons and the finite energy resolution of the detector, these counts do not lead to a well-resolved pile-up peak, but rather to a continuum of counts. For ICR = 4.6 Mcps/pixel, there even seems to be a second continuum of counts at pulse heights above 100 mV, which may represent events in which the pile-up of three X-ray photons gives rise to one count. In addition, a shift of the most probable pulse height toward higher values can be observed for both counting algorithms as the ICR increases. The main difference between the spectra for p-like counting and np-like counting in the top row of Fig. 9 can be observed on the left-hand side of the FWHM bin. If two pulses pile up and the p-like algorithm registers only one count, the np-like algorithm can still detect a second count [see Figs. 2(c) and 3(a)]. This explains why the CRLF for np-like counting in Fig. 6(b) stays closer to 1 than that for p-like counting. However, the maximum signal within the time window of length τ_{np} of the second count will usually be located on the falling edge of a pulse [see Fig. 3(a)]. Consequently, the pulse height associated with this count is typically much lower than the (mean) pulse height corresponding to 60 keV, so the count ends up to the left of the FWHM bin in the spectra. This explains why the spectral performance of the np-like counting algorithm is worse. In the end, a choice between p-like counting and np-like counting depends on whether one prefers better counting or better spectral performance.

For completeness, Fig. 9 also contains the pulse height spectra for the other two values of f_c, i.e., 10 and 5 MHz. In general, the trends observed for $f_c = 20$ MHz can also be seen for these lower f_c. The spectral distortion due to pile-up just gets stronger with decreasing f_c, which manifests as a stronger reduction of the height of the photopeak with increasing ICR, as well as a more dominant presence of the continuum visible on the far right-hand side of the spectra measured at an estimated ICR of 4.6 Mcps/pixel, which may represent events in which three X-ray photons lead to one count.

D. Dedicated Peak Detection Window

The effect of integrating a dedicated peak detection window into the counting algorithms [as described in Section II-D and visualized in Fig. 3(c)] on the pulse height spectra is depicted in Fig. 10(a) for the LYSO:Ce detector with $f_c = 20$ MHz, at an estimated ICR of 4.6 Mcps/pixel. The spectra indicate that the DPDW increases the probability that a registered count ends up inside the FWHM bin rather than to the right-hand side of it. This is reflected in an overall improvement of the SDFs shown in Fig. 10(b) compared to those obtained without DPDW shown in Fig. 8(a).

Fig. 10(a) shows that np-like counting with the dedicated peak detection window also increases the chance that a registered count ends up on the left-hand side of the FWHM bin. Thus, the positive effect of the DPDW is larger for p-like counting than for np-like counting. This is also reflected in the SDFs. Whereas np-like counting with $f_c = 20$ MHz has a better SDF than p-like counting with $f_c = 5$ MHz for the higher values of the ICR in the case without DPDW [see Fig. 8(a)], the SDFs of p-like counting with DPDW are better than those of np-like counting with DPDW regardless of f_c for these values of the ICR [see Fig. 10(b)].

Due to the better spectral performance obtained with the DPDW, higher cut-off frequencies become optimal from a spectral point-of-view at higher values of ICR than before. For example, we note that the SDFs of p-like counting with DPDW for $f_c = 10$ MHz and $f_c = 20$ MHz in Fig. 10(b) are very close to each other over the whole range of investigated ICRs and that $f_c = 20$ MHz only becomes slightly better

than $f_c = 10$ MHz for ICRs exceeding 2.4 Mcps/pixel (was 1.0 Mcps/pixel without DPDW). P-like counting with DPDW and a cut-off frequency of 5 MHz yields the best spectral performance for values of ICR up to 0.7 Mcps/pixel as the inset in Fig. 10(b) shows (was 0.3 Mcps/pixel without DPDW). Nevertheless, we may still conclude that the highest possible value of f_c is most beneficial for practical systems, because it provides better counting performance (see Fig. 6) and the spectral disadvantages at low ICR remain small. This conclusion also remains valid for np-like counting. A choice between p-like counting and np-like counting still depends on whether counting performance or spectral performance is preferred.

Data on the effect of the dedicated peak detection window on the performance of the YAP:Ce detector can be found in the Supplemental Materials. Qualitatively, the same trends as for the LYSO:Ce detector were found, i.e., the values of the ICR for which the different cut-off frequencies are optimal from a spectral point-of-view also increase when using a DPDW. Quantitatively, $f_c = 5$ MHz is optimal until 1.1 Mcps/pixel, $f_c = 10$ MHz between 1.1 and 2.8 Mcps/pixel, and $f_c = 20$ MHz for higher values of ICR in the case of p-like counting with a DPDW, for example, whereas the turning points were at 0.6 and 1.7 Mcps/pixel without a DPDW.

IV. Discussion

We experimentally evaluated the effect of various pulse processing methods on the counting and spectral performance of 1×1 mm^2 single-pixel, ultrafast SiPM-based LYSO:Ce and YAP:Ce scintillation detectors for X-ray photon-counting applications, as a function of ICR/pile-up level. More specifically, we investigated the effect of the cut-off frequency f_c (5, 10, and 20 MHz) of a second-order low-pass filter applied to the raw pulse trains and the effect of p-like and np-like counting algorithms. Evaluating spectral performance is more straightforward with a mono-energetic radiation source, so we placed a 10-GBq Am-241 source (60 keV) at various distances from the detector in order to vary ICR. However, this setup only allowed us to investigate ICRs up to 5 Mcps/pixel. Using LYSO:Ce and YAP:Ce scintillators, we could still achieve interesting pile-up levels at this ICR. However, this also means that these two scintillators are better suited for applications such as cone beam CT in radiotherapy (see Supplemental Materials) than diagnostic CT, for which a faster scintillator, such as $LaBr_3$:Ce, is required [9], [10].

We determined the OCR and the CRLF as a function of ICR in order to evaluate counting performance. As expected, np-like counting with the highest value of f_c is optimal from this point-of-view.

Regarding spectral performance, we first evaluated the traditional measure of the low-rate FWHM energy resolution and found values around 30% at 60 keV for both detectors. A characteristic of the SiPM that has a substantial effect on the achievable energy resolution is the optical photon detection efficiency. The ultrafast SiPMs that we currently use have a relatively low PDE of 20%–30%. However, it is possible to increase the PDE of ultrafast SiPMs to more than 60% [27]. If twice as many optical photons are detected, the energy resolution improves by at best a factor $\sqrt{2}$. Especially the YAP:Ce detector, the energy resolution of which strongly depends on the number of detected scintillation photon due to its proportional response, may therefore obtain an energy resolution closer to 20% FWHM at 60 keV, approaching that of at least one CdTe detector with miniaturized pixels developed for a photon-counting CT prototype [28]. Moreover, many spectral imaging tasks require only two energy bins, which lowers the requirement on the energy resolution. Last but not least, scintillation detectors do not suffer from charge sharing, which deteriorates the spectral performance of CdTe/CZT detectors [15], [29]. Although this is a small effect for pixel sizes of about 1×1 mm^2, it becomes substantial for smaller pixel sizes, such as those used in the first diagnostic photon-counting CT scanners. Also note that the higher number of detected scintillation photons per unit time due to a higher PDE lowers the level of statistical fluctuations on the raw detector pulses, which means that filters with higher values of f_c will output sufficiently smooth pulses, thereby improving the counting performance, too.

We supplemented the traditional measure of the low-rate FWHM energy resolution with the SDF, with the aim to better characterize detector performance under the pile-up conditions that are typically found in X-ray photon-counting applications. The SDF has been defined in (5). It can be seen as an easy-to-calculate measure of spectral performance, providing insight into the fraction of full-energy events that can be considered correctly classified as such under (high) pile-up conditions. We obtained the most favorable SDF values with p-like counting. However, we note that the SDF does not quantify the spread in the energies associated with the counts and that it requires further research to find a relation between SDF values and detector performance in specific imaging tasks. The power of the SDF framework, however, is that it allows for a straightforward (experimental) comparison of prototype detectors (before building a larger-scale imaging system). The alternative is to implement two types of detector in a computer model of an imaging system, and evaluate effects of spectral degradation on image quality in silico. In this context, a recent study by Taguchi et al. [15] is interesting, because it shows that the spectral response of fast scintillators may be better than that of semiconductor (CdTe) detectors for spectral imaging tasks over a wide range of incident fluence rates/pile-up levels.

Another finding of our study is that spectral degradation due to pulse pile-up already kicks in at relatively low ICRs and that, therefore, the FWHM energy resolution at low ICR has limited predictive value for the spectral performance under pile-up conditions. For example, when increasing f_c from 5 to 20 MHz, the FWHM energy resolution of the LYSO:Ce detector at low ICR worsened by about 2 percentage point, while the worsening was about 4 percentage point for the YAP:Ce detector. At the same time, the full width at tenth maximum (FWTM) of the mean detector pulse, which is a typical characteristic of pulse duration, improved from 230 to 132 ns for the LYSO:Ce detector (see Fig. 1) and from 228 to 116 ns for the YAP:Ce detector. As a result, the spectral

detector performance was much less affected by pile-up for $f_c = 20$ MHz. In fact, $f_c = 20$ MHz already appeared optimal from a spectral point-of-view for ICR values greater than a few Mcps/pixel, the exact value depending on the detector and the counting algorithm. This finding may also be applied when selecting an optimal detection material. A faster detection material appears more important than a material that offers somewhat better FWHM energy resolution under low fluence-rate conditions for high-rate spectral X-ray photon-counting applications. Based on an experimental characterization and modeling study presented in [18], benzylamonium lead bromide may be considered a promising example of such an ultrafast scintillator for X-ray photon-counting.

We also found a positive effect of integrating a dedicated peak detection window into the counting algorithms (see Fig. 10). This improvement of spectral performance by determining the pulse height in a short window of length τ_{pd} following the detection of a count [see Fig. 3(c)] is more pronounced for p-like counting than for np-like counting. However, Fig. 5 shows that the lengths of the peak detection windows that we used are rather conservative. About 5 ns lower values of τ_{pd} are possible, which may further improve spectral detector performance.

Lastly, we briefly discuss what is needed to build a pixel array for clinical applications. First, an efficient way to confine the scintillation light to a single pixel is needed, such as thin reflectors (tens of microns [11], [12]) on top of and between scintillator pixels or alternative methods not relying on X-ray insensitive reflectors [13], [14]. Second, an application-specific integrated circuit (ASIC) that operates at the required rate must be developed. First steps in this direction have been taken in [12] and [30]. In this context, it is advantageous that, with good light confinement, there is no need for complicated and resource-intensive corrections, similar to those employed for charge sharing in ASICs for miniaturized semiconductor pixels, which trade off spectral correction and count loss [31], [32]. This may create space and thermal capacity on ASICs for other features, such as more energy bins or the DPDW method investigated in this work.

V. Conclusion

We investigated the counting and spectral performance of two 1×1 mm^2 single-pixel X-ray PCDs based on the fast and widely available LYSO:Ce and YAP:Ce scintillators coupled to an ultrafast SiPM, as a function of input count rate/pile-up level, counting algorithm (p-like/np-like) and cut-off frequency f_c (5, 10, and 20 MHz) of a second-order low-pass filter applied to the raw signals.

Nonparalyzable-like counting in general yields better counting performance than paralyzable-like counting. For $f_c = 20$ MHz, the count-rate loss of both detectors is limited to 10% for ICRs up to 5 Mcps/pixel. However, the spectral performance is generally better for p-like counting. Moreover, we found that spectral degradation due to pile-up kicks in at relatively low ICRs, so that the faster pulses offered by $f_c = 20$ MHz, which yield somewhat worse FWHM energy resolution at low ICR, already provide the best spectral performance at ICRs greater than just a few Mcps/pixel, the exact value depending on the detector and the counting algorithm. We also showed that spectral degradation due to pile-up can be further mitigated by integrating a dedicated peak detection window into the counting algorithms. This is facilitated by the specific shape of the pulses from an SiPM-based scintillation detector.

These findings were obtained using the spectral degradation factor proposed in this work. The SDF supplements the low-rate FWHM energy resolution and quantifies the fraction of full-energy events that can be considered correctly classified as such at any ICR. Thus, the SDF appears to be a useful measure of spectral performance for X-ray PCDs exposed to clinically relevant ICRs.

Our finding that high values of f_c, which lead to fast pulses, are beneficial for both counting and spectral performance from relatively low rates onward, also implies that detection materials that provide considerably faster pulses may yield better SDF values in high-rate applications than those that offer somewhat better low-rate FWHM energy resolution at the expense of a longer pulse duration. This work thus offers guidance for the selection of both suitable detection materials and pulse processing methods for PCDs.

Acknowledgment

All authors thank Stefan Brunner for fruitful discussions about the SiPMs used in this work, and declare that they have no known conflicts of interest in terms of competing financial interests or personal relationships that could have an influence or are relevant to the work reported in this article. The silicon photomultipliers used in this work were supplied in kind by Broadcom Inc.

References

[1] T. Flohr, M. Petersilka, A. Henning, S. Ulzheimer, J. Ferda, and B. Schmidt, "Photon-counting CT review," *Physica Medica*, vol. 79, pp. 126–136, Nov. 2020, doi: 10.1016/j.ejmp.2020.10.030.

[2] S. S. Hsieh, S. Leng, K. Rajendran, S. Tao, and C. H. McCollough, "Photon counting CT: Clinical applications and future developments," *IEEE Trans. Radiat. Plasma Med. Sci.*, vol. 5, no. 4, pp. 441–452, Jul. 2021, doi: 10.1109/TRPMS.2020.3020212.

[3] M. Danielsson, M. Persson, and M. Sjölin, "Photon-counting X-ray detectors for CT," *Phys. Med. Biol.*, vol. 66, no. 3, 2021, Art. no. 03TR01, doi: 10.1088/1361-6560/abc5a5.

[4] M. Persson et al., "Upper limits of the photon fluence rate on CT detectors: Case study on a commercial scanner," *Med. Phys.*, vol. 43, no. 7, pp. 4398–4411, 2016, doi: 10.1118/1.4954008.

[5] K. Rajendran et al., "First clinical photon-counting detector CT system: Technical evaluation," *Radiology*, vol. 303, no. 1, pp. 130–138, 2022, doi: 10.1148/radiol.212579.

[6] S. Si-Mohamed et al., "Feasibility of lung imaging with a large field-of-view spectral photon-counting CT system," *Diagnost. Interv. Imag.*, vol. 102, no. 5, pp. 305–312, 2021, doi: 10.1016/j.diii.2021.01.001.

[7] J. da Silva et al., "Resolution characterization of a silicon-based, photon-counting computed tomography prototype capable of patient scanning," *J. Med. Imag.*, vol. 6, no. 4, 2019, Art. no. 43502, doi: 10.1117/1.JMI.6.4.043502.

[8] U. N. Roy et al., "Role of selenium addition to CdZnTe matrix for room-temperature radiation detector applications," *Sci. Rep.*, vol. 9, no. 1, pp. 1–7, 2019, doi: 10.1038/s41598-018-38188-w.

[9] S. J. van der Sar, S. E. Brunner, and D. R. Schaart, "Silicon photomultiplier-based scintillation detectors for photon-counting CT: A feasibility study," *Med. Phys.*, vol. 48, no. 10, pp. 6324–6338, 2021, doi: 10.1002/mp.14886.

[10] S. J. van der Sar and D. R. Schaart, "Silicon photomultiplier-based scintillation detectors for photon-counting X-ray imaging," in *Radiation Detection Systems*. Boca Raton, FL, USA: CRC Press, 2021, pp. 289–312, doi: 10.1201/9781003147633-10.

[11] F. Godinez, K. Gong, J. Zhou, M. S. Judenhofer, A. J. Chaudhari, and R. D. Badawi, "Development of an ultra high resolution PET scanner for imaging rodent paws: PawPET," *IEEE Trans. Radiat. Plasma Med. Sci.*, vol. 2, no. 1, pp. 7–16, Jan. 2018, doi: 10.1109/TRPMS.2017.2765486.

[12] K. Shimazoe et al., "Performance of custom fine-pitch SiPM-scintillator based photon counting detectors," in *Proc. IEEE Nuclear Sci. Symp., Med. Imag. Conf. Int. Symp. Room-Temp. Semicond. Detect.*, 2023, p. 1, doi: 10.1109/NSSMICRTSD49126.2023.10338002.

[13] L. Bläckberg et al., "Exploring light confinement in laser-processed LYSO:Ce for photon counting CT application," *Phys. Med. Biol.*, vol. 64, no. 9, 2019, Art. no. 95020, doi: 10.1088/1361-6560/ab1213.

[14] S. S. Hsieh, "Activating the interpixel septa of scintillator-photodiode detectors using an X-ray fluorescent reflector material," in *Proc. SPIE Med. Imag., Phys. Med. Imag.*, 2024, pp. 41–44, doi: 10.1117/12.3006477.

[15] K. Taguchi, D. R. Schaart, M. C. Goorden, and S. S. Hsieh, "Imaging performance of a $LaBr_3$:Ce scintillation detector for photon counting X-ray computed tomography: Simulation study," *Med. Phys.*, vol. 52, no. 1, pp. 158–170, 2024, doi: 10.1002/mp.17436.

[16] R. Ballabriga et al., "Review of hybrid pixel detector readout ASICs for spectroscopic X-ray imaging," *J. Instrum.*, vol. 11, no. 1, 2016, Art. no. P01007, doi: 10.1088/1748-0221/11/01/P01007.

[17] S. Surti and J. S. Karp, "Update on latest advances in time-of-flight PET," *Physica Medica*, vol. 80, pp. 251–258, Dec. 2020, doi: 10.1016/j.ejmp.2020.10.031.

[18] J. J. van Blaaderen et al., "$(BZA)_2PbBr_4$: A potential scintillator for photon-counting computed tomography detectors," *J. Lumin.*, vol. 263, Nov. 2023, Art. no. 12002, doi: 10.1016/j.jlumin.2023.120012.

[19] D. N. ter Weele, D. R. Schaart, and P. Dorenbos, "Intrinsic scintillation pulse shape measurements by means of picosecond X-ray excitation for fast timing applications," *Nuclear Instrum. Methods Phys. Res. Sec. A*, vol. 767, pp. 206–211, Dec. 2014, doi: 10.1016/j.nima.2014.08.019.

[20] C. Piemonte and A. Gola, "Overview on the main parameters and technology of modern silicon photomultipliers," *Nuclear Instrum. Methods Phys. Res. A*, vol. 926, pp. 2–15, May 2019, doi: 10.1016/j.nima.2018.11.119.

[21] S. Kappler, A. Henning, B. Kreisler, F. Schoeck, K. Stierstorfer, and T. Flohr, "Photon counting CT at elevated X-ray tube currents: Contrast stability, image noise and multi-energy performance," in *Proc. SPIE Med. Imag., Phys. Med. Imag.*, 2014, pp. 368–375, doi: 10.1117/12.2043511.

[22] R. Steadman, C. Herrmann, and A. Livne, "ChromAIX2: A large area, high count-rate energy-resolving photon counting ASIC for a spectral CT prototype," *Nuclear Instrum. Methods Phys. Res. Sec. A*, vol. 862, pp. 18–24, Aug. 2017, doi: 10.1016/j.nima.2017.05.010.

[23] T. Loeliger, C. Brönnimann, T. Donath, M. Schneebeli, R. Schnyder, and P. Trüb, "The new PILATUS3 ASIC with instant retrigger capability," in *Proc. IEEE Nuclear Sci. Symp. Med. Imag. Conf.*, 2012, pp. 610–615, doi: 10.1109/NSSMIC.2012.6551180.

[24] M. Gustavsson, F. U. Amin, A. Bjorklid, A. Ehliar, C. Xu, and C. Svensson, "A high-rate energy-resolving photon-counting ASIC for spectral computed tomography," *IEEE Transactions on Nuclear Science*, vol. 59, no. 1, pp. 30–39, Feb. 2012, doi: 10.1109/TNS.2011.2169811.

[25] P. Dorenbos, J. T. M. de Haas, and C. Van Eijk, "Non-proportionality in the scintillation response and the energy resolution obtainable with scintillation crystals," *IEEE Trans. Nuclear Sci.*, vol. 42, no. 6, pp. 2190–2202, Dec. 1995, doi: 10.1109/23.489415.

[26] I. V. Khodyuk and P. Dorenbos, "Trends and patterns of scintillator nonproportionality," *IEEE Trans. Nuclear Sci.*, vol. 59, no. 6, pp. 3320–3331, Dec. 2012, doi: 10.1109/TNS.2012.2221094.

[27] E. Engelmann, W. Schmailzl, P. Iskra, F. Wiest, E. Popova, and S. Vinogradov, "Tip avalanche photodiode—A new generation silicon photomultiplier based on non-planar technology," *IEEE Sensors J.*, vol. 21, no. 5, pp. 6024–6034, Mar. 2021, doi: 10.1109/JSEN.2020.3041556.

[28] R. Steadman, C. Herrmann, O. Mülhens, and D. G. Maeding, "ChromAIX: Fast photon-counting ASIC for spectral computed tomography," *Nuclear Instrum. Methods Phys. Res. Sec. A*, vol. 648, pp. S211–S215, Aug. 2011, doi: 10.1016/j.nima.2010.11.149.

[29] K. Stierstorfer and M. Hupfer, "A direct Monte Carlo method for the performance assessment of pixelized detectors," in *Proc. SPIE Med. Imag., Phys. Med. Imag.*, 2024, Art. no. 1292533, doi: 10.1117/12.2690272.

[30] M. Arimoto et al., "Development of 64-channel LSI with ultrafast analog and digital signal processing dedicated for photon-counting computed tomography with multi-pixel photon counter," *Nuclear Instrum. Methods Phys. Res. Sec. A*, 2023, pp. 206–211, doi: 10.1016/j.nima.2022.167721.

[31] O. L. P. Pickford Scienti, J. C. Bamber, and D. G. Darambara, "CdTe based energy resolving, X-ray detector performance assessment: The effects of charge sharing correction algorithm choice," *Sensors*, vol. 200, no. 21, p. 6093, 2020, doi: 10.3390/s20216093.

[32] K. Taguchi and J. S. Iwanczyk, "Assessment of multi-energy inter-pixel coincidence counters for photon-counting detectors at the presence of charge sharing and pulse pile-up: A simulation study," *Med. Phys.*, vol. 48, no. 9, pp. 4909–4925, 2020, doi: 10.1002/mp.15112.